Dalton Transactions

PAPER

Evidence of low dimensional ion transport in mechanosynthesized nanocrystalline BaMgF₄

F. Preishuber-Pflügl* and M. Wilkening

Mechanochemical milling provides a versatile method for the preparation of nano-sized, defect rich, polycrystalline materials. If ionic materials are considered, the transport parameters of the mobile ions may greatly differ from those of the microcrystalline counterparts prepared by conventional synthesis routes. Little is known about ionic conduction in nanocrystalline materials having crystal structures that offer spatially confined transport pathways. Here, we focused on mechanosynthesized $BaMgF_4$ that combines both nanocrystallinity and anisotropic F^- transport. The preparation of nanocrystalline $BaMgF_4$ is presented as a facile and rapid one-pot procedure. The reaction was followed by X-ray diffraction and high-resolution ^{19}F nuclear magnetic resonance (NMR) spectroscopy. NMR helped prove the formation of X-ray amorphous compounds as well as the transformation of the starting materials into the final product $BaMgF_4$. Most importantly, besides enhanced conduction properties compared to a single crystal, our broadband impedance spectra reveal characteristics pointing to anisotropic (low dimensional) ion transport processes even in the nanocrystalline form of $BaMgF_4$.

Introduction

Adaptable synthesis techniques provide the basis for the development of new functional materials which are crucially needed for, *e.g.*, new sensors, catalysts or powerful energy storage systems taking advantage of solid state ion conductors. High-energy ball-milling has been proven to be a highly versatile method for the preparation of nanocrystalline solids with extraordinary micro- as well as macroscopic properties such as optical, electrical or magnetic behaviour.[1,2]

In many cases, but not in all, nanocrystalline materials prepared in this way show enhanced ion transport properties.[2,3] Increased ion dynamics is directly linked with the great amount of defects introduced during mechanical treatment.[3,4] The different types of defects generated determine both bulk properties as well as those related to the large volume fraction of interfacial regions (or grain boundaries). Compared to their coarse-grained or single crystalline counterparts, the mean crystallite diameter of cluster-assembled nanocrystalline ceramics is smaller than 50 nm. Their various properties are governed by the large number fraction of ions in or near the interfacial regions, that is, the surface-influenced volume. Depending on the thickness of the surface layer, which may range from 0.5 to 2 nm, for a mean crystallite size of approxi-

mately 20 nm up to 20 to 30% of the ions may reside in the interfacial regions. As an example this has been shown for Li-bearing nanocrystalline oxides such as Li_2O and $LiNbO_3$.[2,3] Besides the preparation of thermodynamically stable compounds, in the extreme case mechanochemistry also provides access to metastable and nanocrystalline phases that cannot be prepared *via* conventional synthesis routes requiring high temperatures, see, *e.g.*, ref. 5–8.

Although a huge number of studies can be found focusing on the synthesis and characterization of nanocrystalline ion conducting ceramics,[2] investigations putting emphasis on ion dynamics in nanocrystalline conductors crystallising with structures that offer spatially confined transport pathways are scarce. Little is known how anisotropic transport is altered when such materials have been prepared in a nanocrystalline form *via* mechanosynthesis. Here, ferroelectric $BaMgF_4$, crystallising with the orthorhombic $BaZnF_4$ structure (space group $Cmc2_1$, see Fig. 1), was chosen as a suitable model system combining these two aspects.

In its single crystalline form, the ternary fluoride reveals highly anisotropic ion conduction. This was shown by Kannan *et al.*[9] who investigated ion transport at high temperatures by means of impedance spectroscopy. The authors report on enhanced conductivity along the *c*-axis of a single crystal, which enables fluorine ions to jump *via* vacant sites along the corner sharing octahedra.[10] In $BaMgF_4$ the MgF_6 octahedra are linked *via cis* vertices to zigzag chains parallel to the *c*-axis; along the *a*-axis, these chains are connected *via trans* vertices to slabs parallel to the *ac*-plane. The same anisotropy in ion

Graz University of Technology, Institute for Chemistry and Technology of Materials (Member of NAWI Graz), Stremayrgasse 9, 8010 Graz, Austria. E-mail: preishuber-pfluegl@tugraz.at
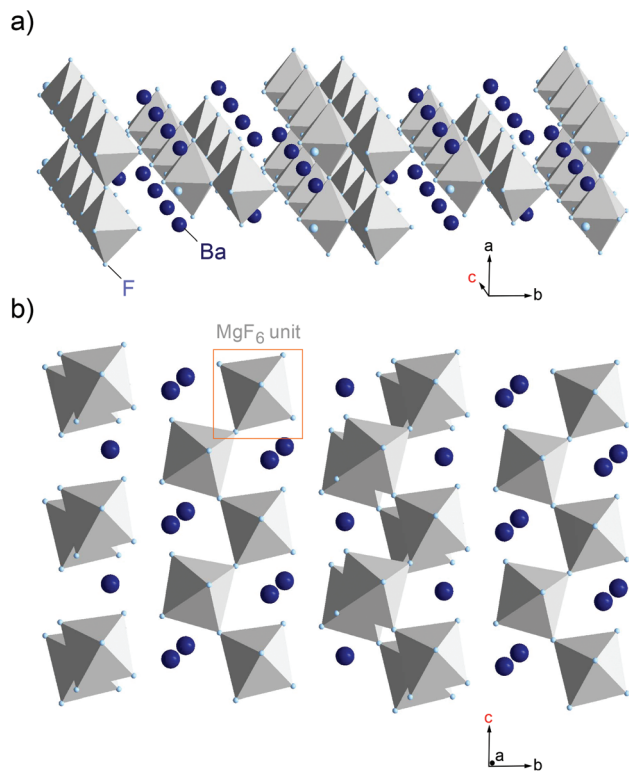
a)

b)

Fig. 1 Crystal structure of BaMgF$_4$ (space group $Cmc2_1$,) illustrating the connectivity of the MgF$_6$ octahedra and the anisotropic migration pathway of the F anions along the c-axis.

conduction has also been found for BaMnF$_4$ and other compounds of this isomorphic family. From an application point of view, BaMgF$_4$ is known as a promising material for all-solid-state laser applications;[11] moreover, it is a candidate for non-destructive readout ferroelectric random access memory devices using metal–ferroelectric–semiconductor structures.[12]

In the present study, it was synthesized *via* ball-milling directly from the binary fluorides BaF$_2$ and MgF$_2$. The reaction was carried out as a one-pot procedure yielding a phase-pure powder already after three hours of milling; no further purification or annealing steps were necessary. The convenience of this versatile synthesis route also highlights the benefits of mechanochemistry compared to other methods such as high temperature solid-state synthesis, including hydrothermal routes, sol–gel reactions or wet chemical methods.[13–17]

Compared to single crystalline BaMgF$_4$ we found enhanced ion transport properties for the nanocrystalline form investigated here. Permittivity and conductivity spectra are discussed in terms of electrical responses resulting from bulk and grain boundary regions. Interestingly, even in the case of a nanocrystalline, mechanosynthesized sample, the frequency-dependent conductivity measurements carried out point to low dimensional ionic conduction along the c-axis. This can be inferred from the shallow frequency dependence in the dispersive regions of the conductivity isotherms. Such features have only

rarely been used to enlighten the effect of dimensionality of a given hopping process on the frequency dependence of conductivity values.[18]

Experimental section

Materials and methods

BaMgF$_4$ was synthesized by mechanical treatment of the binary fluorides in a high-energy ball mill (Fritsch Pulverisette 7 premium line). Stoichiometric amounts of BaF$_2$ and MgF$_2$ were milled using 180 balls made of zirconium dioxide (ZrO$_2$) with a diameter of 5 mm in beakers of the same material. The ball-to-powder ratio was set to 14 : 1. To exclude any moisture and the influence of any oxygen during milling, the powders and beakers were strictly handled in a glovebox filled with a dry argon atmosphere (O$_2$ and H$_2$O < 0.5 ppm). If not stated otherwise, the total milling time was set to three hours consisting of 36 cycles à five minutes, each one followed by a resting interval of 25 minutes allowing the beakers to cool down. After each hour of milling, *i.e.*, after twelve cycles, the beakers were opened and the powder was completely removed and homogenized in an agate mortar; then, the samples for X-ray diffraction (XRD) and magic angle spinning nuclear magnetic resonance (MAS NMR) analysis were taken, see Fig. 2. It should be mentioned that the amount of the samples taken out was very small in order not to change the ball to powder ratio.

Structural characterisation of the resulting powders was carried out on a Bruker D8 Advance diffractometer with Bragg Brentano geometry using Cu Kα radiation (10 to 100° 2θ, step size 0.02° 2θ, step time 1 s). Rietveld-refinement was done with X-PertHighScorePlus (PANalytical). ^{19}F MAS NMR experiments were recorded on a Bruker Avance III spectrometer operating at 470.4 MHz employing a 2.5 mm-MAS probe (Bruker) being able to reach a maximum spinning speed of 30 kHz. Spectra were referenced to solid, crystalline LiF (−204.3 ppm) serving as a secondary standard (primary reference CFCl$_3$, 0 ppm), see Fig. 2(b). Spectra were recorded after non-selective excitation with a single radio-frequency pulse; the pulse length was 2 μs. After Fourier transformation of the free induction decays, phase correction in first and second order was carried out using TopSpin software and MestreNova.

For our dielectric measurements, 200 mg of the powder were pressed in a mould with 10 mm inner diameter applying a uniaxial pressure of 0.13 GPa yielding pellets of about 1 mm in thickness, each time measured with an appropriate caliper. 100 nm of gold, serving as electrodes, were applied on both sides of the pellet with a sputter coater (Leica) to ensure good electrical contact. Impedance spectra (see Fig. 3) were measured with a Novocontrol Concept 80 broadband analyser (Alpha-AN, Novocontrol) using a BDS 1200 cell in combination with an active ZGS cell interface (Novocontrol) allowing temperature-variable two-electrode (dielectric) measurements. Frequencies covered a range of nine decades, starting from 10^{-2} Hz up to 10 MHz. The temperature was varied between
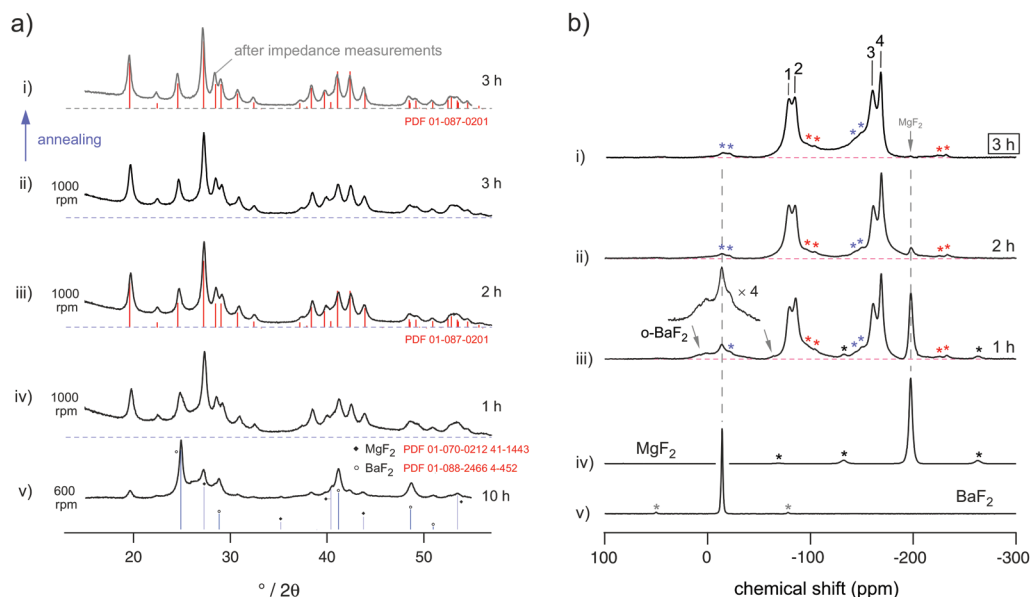
Fig. 2 (a) X-ray powder diffraction patterns of the ball-milled reaction mixture after 1 h, 2 h, and 3 h of milling at 1000 rpm in ZrO$_2$ beakers; reflections of a BaMgF$_4$ single crystal are indicated by vertically drawn (red) lines.: The patterns are stacked with a constant pitch. For comparsion, the powder pattern obtained when the milling conditions are changed to 600 rpm and 10 h, that is lower mechanical impact but longer milling time, is also shown, see (v). The pattern labelled (i) is obtained after impedance measurements. (b) ^{19}F MAS NMR spectra of the reaction mixture at different stages of milling. Spectra were recorded at a spinning speed of 30 kHz. Asterisks indicate the various spinning side bands of the BaMgF$_4$ signal as well as those originating from the starting materials. (iv) and (v) show reference NMR spectra of the non-treated starting materials BaF$_2$ and MgF$_2$. Small arrows indicate those NMR lines that can be assigned to orthorhombic BaF$_2$. In (iii) the region from 50 ppm to $-$50 ppm is enlarged to illustrate additional NMR intensities near the ^{19}F signal of BaF$_2$.

133 and 573 K in steps of 10 K; it was automatically controlled by a QUATRO cryosystem (Novocontrol). A dry nitrogen atmosphere with the appropriate temperature is built up around the sample in the cryostat by a constant flow of gas, freshly evaporated from a dewar containing liquid nitrogen.

Results and discussion

Sample characterisation by X-ray diffraction

Fig. 2(a) shows the X-ray powder diffraction patterns of the resulting nanocrystalline materials after treating the binary fluorides, BaF$_2$ and MgF$_2$, over an increasing amount of time in a planetary mill at 1000 rounds per minute (rpm). Already after one hour (see the pattern labelled (iv)), the diffraction pattern solely reveals the formation of only one phase *viz* orthorhombic BaMgF$_4$. Broad background signals, however, show up at small diffraction angles that indicate the presence of a certain amount of amorphous material. This could either result from amorphous BaF$_2$ and/or MgF$_2$ formed under the harsh milling conditions or from abrasion of zirconium dioxide from the milling tools. The former explanation is supported by our NMR measurements (see below); residues of the starting materials become X-ray amorphous; however, they can be identified by ^{19}F MAS NMR. It turned out that the isotropic chemical shifts of amorphous BaF$_2$ and MgF$_2$ are almost identical with those of the crystalline counterparts. The same has been found previously for pure, nanocrystalline BaF$_2$.[6] Of course, XRD reflections with weak intensity belonging to the

binary fluorides could be hidden by the broadened signals of BaMgF$_4$ governing the pattern. It is worth mentioning that lowering the mechanical impact, *i.e.*, using 600 rpm instead of 1000 rpm, does not lead to a complete formation of BaMgF$_4$ even if the milling time is increased from 1 h to 10 h. This is illustrated by the X-ray powder pattern (v) included in Fig. 2(a).

The mean crystallite size of our samples treated at 1000 rpm ranges from about 10 nm after one hour of milling to about 7 nm to 15 nm after three hours. These values have been estimated using the equation introduced by Scherrer with a shape factor of 0.9 representing spherical crystallites. They do not take into account the influence of strain generated during milling; such an effect, however, does not change the estimated values much as has been shown by previous studies on similar fluorides.[8,19]

In Table 1 the cell parameters obtained from Rietveld refinement are listed. Compared to the results on BaMgF$_4$ single crystals,[20] ball milling leads to a slight distortion of the cell geometry; the position of the reflections are marginally shifted towards larger diffraction angles. In spite of that, the decrease of the Bragg factor R_{Bragg} with increasing milling time reveals that the resulting structure increasingly resembles that of BaMgF$_4$ described in the literature.[20]

Further characterisation by high-resolution solid-state ^{19}F NMR spectroscopy

Compared to X-ray diffraction, MAS NMR spectroscopy allows more distinct insights into the mechanochemical reaction pro-
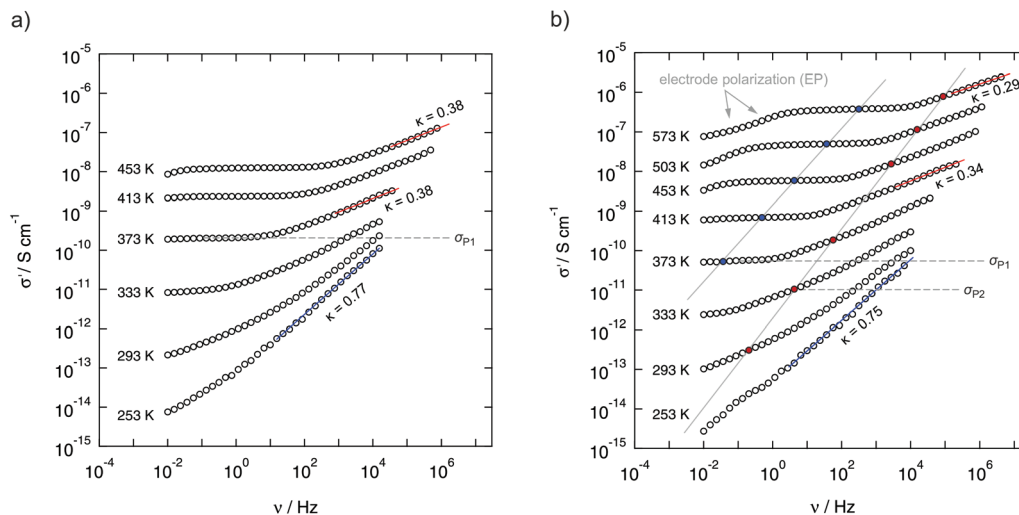
Fig. 3 Conductivity isotherms (real part of complex conductivity *vs.* frequency) recorded of the sample obtained after three hours of milling. (a) Data obtained from the second heating run up to 473 K and (b), from the third heating run up to 573 K. All the spectra shown reveal characteristic dc-conductivity plateaus at elevated temperatures. Additional plateaus, however, show up at higher frequencies. They are highlighted in (b) by red circles. Conductivities at the highest frequencies can be approximated with power laws. κ values indicate the corresponding power law exponents. Arrows in (b) mark polarisation effects due to the ion blocking electrodes applied.

Table 1 Lattice parameters of the mechanosynthesized powders as obtained from Rietveld refinement; data for the $BaMgF_4$ single crystal listed were taken from ref. 20

Milling time/h	a/Å	b/Å	c/Å	R_{Bragg}
1	4.146(1)	14.479(1)	5.814(1)	9.2
2	4.141(1)	14.489(1)	5.813(1)	6.4
3	4.139(1)	14.495(1)	5.810(1)	5.5
Single crystal	4.126	14.518	5.821	—

cedure; the evolution of the characteristic $BaMgF_4$ NMR signals and the decrease of the corresponding intensities of the starting materials is clearly outlined in the spectra shown in Fig. 2(b).

By using a rotation frequency of 30 kHz, four different fluorine sites, being crystallographically and magnetically inequivalent, can be distinguished *via* MAS NMR: −79.5 ppm (1), −85.1 ppm (2), −160.6 ppm (3) and −168.6 (4) ppm, see Fig. 2(b) (i) to (iii), the NMR lines are indicated by numbers. These values are in good agreement with results from other studies reported in the literature but focusing on, *e.g.*, single crystalline and polycrystalline $BaMgF_4$ synthesized *via* solid state pathways.[13] Once again, this comparison shows that ^{19}F NMR chemical shifts of nanocrystalline mechanosynthesized fluorides do not differ much from those of crystalline materials. In our case, however, the ^{19}F MAS NMR lines are considerably broadened, pointing at significant structural disorder due to the enormous mechanical impact during milling.

Besides the formation of the desired ternary fluoride, which shows up already after just 1 hour of milling, in the early stages of mechanical treatment NMR lines of orthorhombic BaF_2 show up. This behaviour was also observed previously for pure BaF_2 prepared in a similar way.[5,6,8] Orthorhombic BaF_2 is a high pressure phase of barium fluoride which forms under

the milling conditions chosen here.[5] With increasing milling time, however, it is completely transformed into $BaMgF_4$.

Regarding the ppm region from 20 ppm to −50 ppm in more detail (Fig. 2(b), (iii)), additional NMR lines with low intensity show up after one hour of milling. They cannot be completely assigned to the formation of orthorhombic BaF_2. Most likely, these intensities point to ^{19}F chemical shifts of a small amount of (X-ray amorphous) Mg doped cubic-BaF_2 that might represent the initial reaction product which is then continuously transformed into $BaMgF_4$.

After three hours of milling, the NMR lines of BaF_2 and MgF_2 as well as the weak signals of the side products completely disappeared. Compared to our experiments performed at only 600 rpm, the preparation of pure $BaMgF_4$, as it is carried out here, is driven by the higher mechanical impact at 1000 rpm leading to increased grinding and local pressure. Additionally, the effect of hot spots may further support the transformation of BaF_2 and MgF_2 into phase pure $BaMgF_4$. For comparison with other synthesis routes, the high rotation speed of 1000 rpm leads to a temperature increase from room temperature to approximately 370 K inside of the beakers. A precise value of temperature and pressure, giving clear insights into the reaction conditions inside the milling beakers cannot be given as our current synthesis equipment does not support a measurement of these values. Here, we roughly estimated the inner temperature from measurement on the outer surface of the beakers.

Ion dynamics probed by temperature-variable impedance and dielectric measurements

The dielectric response of mechanosynthesized $BaMgF_4$ was investigated at temperatures ranging from 133 K to 573 K over a broad frequency range (ν = 10 mHz to 10 MHz) covering nine
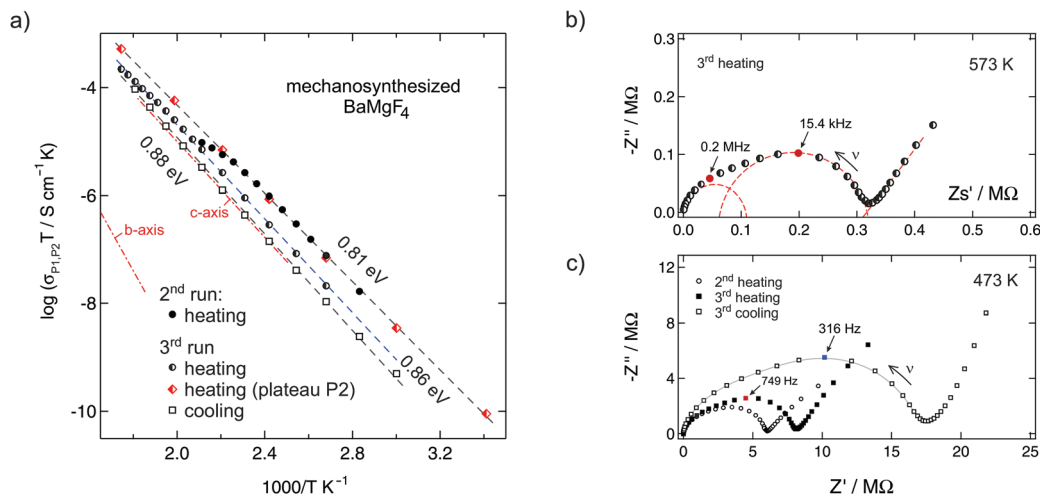
Fig. 4 (a) Arrhenius diagram showing the temperature dependence of the dc–conductivity and of the additional plateau value of Fig. 3. (b). The dashed lines show Arrhenius fits. For comparison, the dashed–dotted line represents the conductivity of a single crystal along the *b*-axis; the values for conduction along the *c*-axis coincide with our data found for the third cooling cycle. (b, c) Complex plain plots of the real part *vs.* the imaginary part of the impedance show depressed, overlapping semi-circles for the ball milled, nanocrystalline samples. The coloured symbols (to which the arrows point) represent the frequency at the maximum of the semicircle. (b) The red, dashed semicircles schematically represent two different diffusion processes corresponding to the plateaus P1 and P2 in Fig. 3(b). (c) The grey, solid line serves as a guide to the eye.

decades (see Fig. 3 and 4). This enabled us to get detailed insights into the length-scale dependent ion dynamics in the nanocrystalline ternary fluoride providing a channel-like arrangement for some of the fluorine ions. This constraint of a crystal structure is a prerequisite for low-dimensional diffusion. Quasi 1D ionic transport has been proposed by Kannan *et al.*[9] based on impedance spectroscopy results on BaMgF$_4$ single crystals; ionic transport along the *c*-axis is reported to be much faster than that along the *b*-axis. Such low-dimensional hopping of the mobile charge carriers should become apparent as a characteristic signature in the dispersive regime of $\sigma'(\nu)$ of the conductivity isotherms.[18] Here, σ' denotes the real part of the complex conductivity. Specifically, a relatively shallow frequency dependence $\sigma'(\nu) \approx \nu^\kappa$ is expected for low dimensional ion conduction with the Jonscher exponents κ being (significantly) smaller than approximately 0.5.[18]

The conductivity isotherms shown in Fig. 3 are composed of four regimes. (i) At low frequencies (and sufficiently high temperatures and thus ion mobility) electrode polarisation (EP) effects show up owing to the pile-up of ions near the surface of the blocking Au electrodes applied. In many cases a step-wise decay of σ' is detected (see the two arrows in Fig. 3(b)). (ii) The polarisation regime passes over into a distinct conductivity plateau (P1) governing the isotherms at intermediate temperatures and low frequencies. If this plateau is identified with a bulk response, it reflects long-range ion transport and is called the dc-plateau. Moving to higher frequency a shallow dispersive regime with a weak frequency dependence shows up. It directly merges into a shallow second plateau (iii, P2) passing over in the final dispersive regime (iv) which can be approximated with a Jonscher power law (see above). The second plateau becomes clearer in the third heating run as

can be seen by the isotherms shown in Fig. 3(b). In that figure the temperature-dependent levels of the plateaus P1 and P2 on the ordinate are highlighted by filled circles. The same characteristics do also show up in the corresponding permittivity spectra presented in Fig. 5 and discussed below.

To analyse the conductivity data in terms of dimensionality effects we looked at the Jonscher exponents of the dispersive regime. At low temperatures the exponent κ takes values of approximately 0.75 (see Fig. 3(a) and (b)). Most likely, strongly correlated motion or spatially localized ones already influence $\sigma'(\nu)$. The prominent nearly-constant-loss phenomenon, see ref. 21 for an overview, being frequently related to caged dynamics in so-called asymmetric double well potentials, would lead to κ values close to one.

Most importantly, at higher temperatures, that is above 333 K, the exponent κ drops below 0.4 and less. As mentioned above, this gives evidence for a low dimensional transport process. As summarized in ref. 18, such low Jonscher exponents seem to be characteristic for 1D and 2D diffusion as is found in beta-alumina and other low-dimensional ion conductors.

In order to underpin the interpretation of κ as being an indicator of low-dimensional transport in BaMgF$_4$, we compared the conductivity values of the two plateaus of our isotherms with the corresponding values of Kannan *et al.*[9] who carried out orientation-dependent measurements on single crystals. In the Arrhenius plot of Fig. 4 the σ' values of the first plateau P1 are shown, which have been read out from the isotherms of different heating runs. Heat treatment at elevated temperatures causes a continuous decrease of ion conductivity, which is presumably due to healing of defects and/or thermal equilibration. At the top of each heating cycle, the conductivity
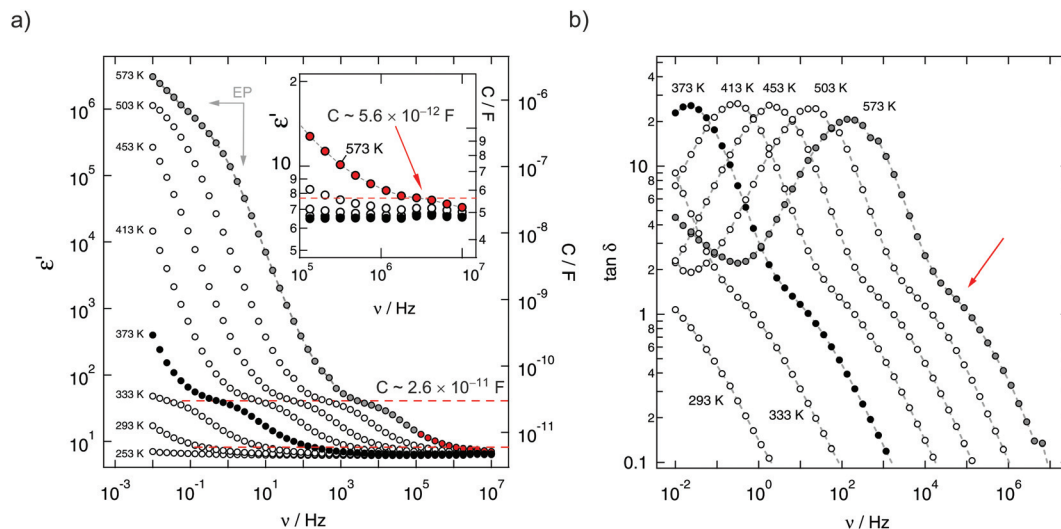
Fig. 5 (a) Real part of the permittivity as a function of frequency showing two distinct plateaus with characteristic capacities for bulk conduction processes, see the horizontally drawn dashed lines. This is particularly illustrated in the inset; see the isotherm recorded at 573 K. (b) Plot of the dielectric loss, tan δ, *versus* frequency, likewise showing an additional peak as a shoulder in the spectra as indicated by the arrow. EP denotes contributions from electrode polarisation.

drops slightly, and when going back to lower temperature the slope of the dashed lines in Fig. 4(a) increases reflecting an increase of the corresponding activation energy E_A.

In order to explore possibly origins of this behaviour we recorded an X-ray powder pattern after heat treatment in the impedance cell, see the pattern at the top of Fig. 2(a). The remaining broad reflections do not indicate any significant grain growth. Therefore, local changes, that is a reduction of the concentration of defects, might be responsible for the change in conductivity rather than macroscopic ones. The amount of amorphous material seems to be somewhat reduced compared to the pattern directly recorded after mechanosynthesis of BaMgF$_4$.

Coming back to Fig. 4(a) the dashed lines represent fits with an Arrhenius law according to $\sigma T_{P1,P2} \propto \exp(-E_A/(k_B T))$; k_B denoting Boltzmann's constant. Starting from 0.81 eV the activation energy E_A slightly increases to 0.88 eV after the sample has been exposed to 473 K for about 1 h inside the impedance cell. Interestingly, the values measured for the third run (cooling from 473 K to lower T) coincide with those reported for ion conduction along the c-axis in BaMgF$_4$ as reported by Kannan *et al.*[9] Along this axis, the MgF$_6$-octahedra are directly connected forming a low-dimensional diffusion pathway (see also Fig. 1). Ion conduction along the b-axis is indicated in Fig. 4(a) by a dashed line; in contrast to fast ion movement along the c-axis, ion transport is much slower.

Besides the conductivity values of the first plateau, those of the second one are also included in Fig. 4. The data points follow an activation energy of approximately 0.81 eV (3rd run, heating). Regarding absolute conductivity values, they are by about one order of magnitude larger than those reported for ion conduction along the c-axis in BaMgF$_4$ single crystals.[9]

To illustrate the presence of a second conductivity plateau in another way, we also analysed the corresponding Nyquist plots which can be constructed when the real part of the impedance Z' is plotted *vs.* the imaginary part Z''. Exemplarily, data recorded at 473 K are shown in Fig. 4(c). The Nyquist curves are clearly composed of two overlapping semicircles reflecting the two plateaus (P1 and P2) of the $\sigma'(\nu)$ isotherms. With each heating run the intercepts (with the Z'-axis) of the two, slightly depressed semicircles shift towards higher impedances $Z' \propto 1/\sigma'$ (Fig. 4(c)); this is, of course, also represented by the conductivities (see Fig. 4(a)).

The fact that the overall impedance response is composed of three different regions can be best seen in Fig. 4(b) that shows the Nyquist curve recorded at 573 K. While the spike at the lowest frequencies represent electrode polarisation, the two semicircles can be relatively well separated from each other. For comparison, the same two different dielectric responses can also be seen when the real part of the complex permittivity ε' or the dielectric loss tan δ is plotted *vs.* frequency (see Fig. 5(a) and (b)). The response of tan δ obviously reveals a shoulder at higher frequencies; it is exemplarily indicated by the arrow in Fig. 5(b) and points to the second relaxation process P2.

In order to judge if and to which extent any grain boundary effects govern the low-frequency response, that is the P1 conductivity plateau, we looked at the corresponding capacities C_i (i = P1, P2). From the $\varepsilon'(\nu)$ isotherms, it can be read out that the capacity C_{P2} of the high frequency response, corresponding to the second σ' plateau, is about 5.6(5) pF clearly proving bulk ion conduction. The response at lower frequencies, corresponding to the first conductivity plateau, is approximately given by C_{P1} = 26(2) pF. To our opinion, this value is

in between that for bulk and grain boundary response; we tend to interpret it as a bulk response which is already affected by the surface-influenced volume of our nanocrystalline sample.

Lastly, almost the same values for C_i can be determined from the Nyquist plots if two RC-circuits connected in series are simply used to analyse the complex plane data. According to the maximum condition $\omega_{max}RC = 1$, with $\omega_{max} = 2\pi\nu$, the capacities are 5(1) pF and 40(5) pF, respectively. Furthermore, the conductivities, calculated from the resistances R_{P1} and R_{P2} of the intercepts with the Z'-axis, confirm the values determined from the $\sigma'(\nu)$ isotherms (see the two lines in Fig. 3 connecting the filled circles of plateau P1 and P2, respectively). Thus, as mentioned above, compared with the results from BaMgF$_4$ single crystals, even after soft annealing of the freshly prepared sample in the impedance cell *in situ*, ion transport is somewhat enhanced in the nanocrystalline form (see (red) diamonds in Fig. 4(a)).

Conclusions and outlook

Polycrystalline BaMgF$_4$ was successfully synthesized *via* a one-pot mechanochemical route. Apart from structural characterization by X-ray diffraction, ^{19}F MAS NMR spectroscopy was employed to directly track the local magnetic changes around the F spins. NMR indicates a reaction mechanism that initially involves the incorporation of MgF$_2$ into the cubic structure of BaF$_2$ which finally transforms into the desired product *viz* orthorhombic BaMgF$_4$.

Conductivity spectroscopy and permittivity spectroscopy as well reveal two distinct ion transport processes. The associated capacities as estimated from the corresponding Nyquist plots may be interpreted as electrical responses originating from the bulk and grain boundary affected regions. Absolute conductivities of the two processes differ by a factor of approximately ten; this trend is in line with the corresponding activation energies of the two processes, 0.81 eV *vs.* 0.88 eV. Thus, from a microscopic point of view the underlying ion hopping processes might be very similar. If compared with previous measurements on single crystals of BaMgF$_4$, ionic conductivity probed here resembles that being characteristic along the *c*-axis; ion dynamics along the *b*-axis is reported to be much slower.

Most importantly, if analysed in terms of Jonscher exponents, the frequency dependent conductivity measurements point to low-dimensional ionic conduction even in the nanocrystalline form of BaMgF$_4$. Relatively small exponents have also been presented in the literature for, *e.g.*, sodium ion conduction in beta-alumina showing 2D diffusion.

In order to investigate the origin of the different conduction processes of our nanocrystalline material, the influence of sintering on both grain growth and ion dynamics will be the subject of further studies. These will also include ^{19}F NMR relaxometry in both the laboratory and in the rotating frame of reference to throw light on F ion dynamics taking place on different length scales.

Notes and references

1 V. Šepelák, A. Düvel, M. Wilkening, K. D. Becker and P. Heitjans, *Chem. Soc. Rev.*, 2013, **42**, 7507.

2 P. Heitjans and S. Indris, *J. Phys.: Condens. Matter*, 2003, **15**, R1257.

3 P. Heitjans, M. Masoud, A. Feldhoff and M. Wilkening, *Faraday Discuss.*, 2007, **134**, 67.

4 M. Wilkening, V. Epp, A. Feldhoff and P. Heitjans, *J. Phys. Chem. C*, 2008, **112**, 9291.

5 B. Ruprecht, M. Wilkening, S. Steuernagel and P. Heitjans, *J. Mater. Chem.*, 2008, **18**, 5452.

6 B. Ruprecht, M. Wilkening, A. Feldhoff, S. Steuernagel and P. Heitjans, *Phys. Chem. Chem. Phys.*, 2009, **11**, 3071.

7 A. Düvel, B. Ruprecht, P. Heitjans and M. Wilkening, *J. Phys. Chem. C*, 2011, **115**, 23784.

8 A. Düvel, S. Wegner, K. Efimov, V. Šepelák, P. Heitjans and M. Wilkening, *J. Mater. Chem.*, 201, **21**, 6238.

9 C. V. Kannan, K. Shimamura, H. R. Zeng, H. Kimura, E. G. Villora and K. Kitamura, *J. Appl. Phys.*, 2008, **104**, 114113.

10 J. F. Scott, *Rep. Prog. Phys.*, 1979, **42**, 1055.

11 E. G. Villora, K. Shimamura, K. Sumiya and H. Ishibashi, *Opt. Express*, 2009, **7**, 12362; K. Shimamura, E. G. Villora, H. R. Zeng, M. Nakamura, S. Takekawa and K. Kitamura, *Appl. Phys. Lett.*, 2006, **89**, 232911; E. G. Víllora, P. Molina, S. Álvarez, J. V. García-Santizo, M. O. Ramírez, K. Shimamura and L. E. Bausá, *J. Appl. Phys.*, 2010, **107**, 033106; Y. Ma, J. Chen, Y. Zheng and X. Chen, *Appl. Opt.*, 2012, **51**, 5432; T. E. Littleford, R. A. Jackson and M. S. D. Read, *Phys. Status Solidi C*, 2013, **10**, 153; L. Mateos, M. O. Ramírez, I. Carrasco, P. Molina, J. F. Galisteo-López, E. G. Víllora, C. de las Heras, K. Shimamura, C. Lopez and L. E. Bausá, *Adv. Mater.*, 2014, **24**, 1509.

12 S. Sinharoy, H. Buhay, M. H. Francombe, W. J. Takei, N. J. Doyle, J. H. Rieger1, D. R. Lampe and E. Stepke, *J. Vac. Sci. Technol., A*, 1991, **9**, 409.

13 R. M. Kowalczyk, T. F. Kemp, D. Walker, K. J. Pike, P. A. Thomas, J. Kreisel, R. Dupree, M. E. Newton, J. V. Hanna and M. E. Smith, *J. Phys.: Condens. Matter*, 2011, **23**, 315402; M. Body, G. Silly, C. Legein and J.-Y. Buzaré, *J. Phys. Chem. B*, 2005, **109**, 10270.

14 U. Groß, S. Rüdiger and E. Kemnitz, *Solid State Sci.*, 2007, **9**, 838.

15 S. Fujihara, S. Ono, Y. Kishiki, M. Tada and T. Kimura, *J. Fluorine Chem.*, 2000, **105**, 65.

16 P. D. Belsare, C. P. Joshi, S. V. Moharil, S. K. Omanwar, P. L. Muthal and S. M. Dhopte, *J. Alloys Compd.*, 2008, **464**, 296.

17 S. W. Kim, H. Y. Chang and P. S. Halasyamani, *J. Am. Chem. Soc.*, 2010, **132**, 17684.

18 D. L. Sidebottom, *Phys. Rev. Lett.*, 1999, **83**, 983.

19 A. Düvel, M. Wilkening, R. Uecker, A. Feldhoff and P. Heitjans, *Phys. Chem. Chem. Phys.*, 2010, **12**, 11521.

20 F. Gingl, *Z. Anorg. Allg. Chem.*, 1997, **623**, 705.

21 K. Funke, C. Cramer and D. Wilmer, in *Diffusion in Condensed Matter – Methods, Materials, Models*, ed. P. Heitjans and J. Kärger, Springer, Berlin, 2nd edn, 2005, ch. 21, pp. 857–893.